

Review

# Optoelectronic Devices Based on Atomically Thin Transition Metal Dichalcogenides

Andreas Pospischil \* and Thomas Mueller

Institute of Photonics, Vienna University of Technology, 1040 Vienna, Austria; thomas.mueller@tuwien.ac.at

\* Correspondence: andreas.pospischil@tuwien.ac.at; Tel.: +43-1-58801-38725

Academic Editor: Andres Castellanos-Gomez

Received: 10 February 2016; Accepted: 7 March 2016; Published: 10 March 2016

**Abstract:** We review the application of atomically thin transition metal dichalcogenides in optoelectronic devices. First, a brief overview of the optical properties of two-dimensional layered semiconductors is given and the role of excitons and valley dichroism in these materials are discussed. The following sections review and compare different concepts of photodetecting and light emitting devices, nanoscale lasers, single photon emitters, valleytronics devices, as well as photovoltaic cells. Lateral and vertical device layouts and different operation mechanisms are compared. An insight into the emerging field of valley-based optoelectronics is given. We conclude with a critical evaluation of the research area, where we discuss potential future applications and remaining challenges.

**Keywords:** 2D materials; transition metal dichalcogenides; optoelectronic devices

## 1. Introduction

The rediscovery of graphene by Geim and Novoselov [1] has led to renewed interest in layered materials. Beyond graphene, hundreds of other layered materials exist that can be thinned down into monolayers [2]. One important family of two-dimensional (2D) materials is the family of layered transition metal dichalcogenides (TMDs). In their bulk form, TMDs have been studied for decades [3,4], but the properties of TMD monolayers differ significantly from their bulk characteristics. For example, a layer-dependent indirect-to-direct bandgap transition is commonly observed in TMD semiconductors, which results in bright light emission from monolayers, whereas emission from bulk crystals is practically absent. This and other interesting properties have recently fueled intensive research efforts on TMD-based optoelectronic devices, which have already led to several promising new device concepts.

## 2. Basic Optical Properties

TMDs have the chemical formula  $MX_2$ , where  $M$  is a transition metal (e.g., Mo, W, etc.) and  $X$  is a chalcogen atom (S, Se, or Te) [5–9]. The atoms in 2D TMDs are arranged in an  $X$ – $M$ – $X$  sandwich, with a monolayer thickness of 0.6–0.7 nm. For optoelectronic devices, mainly Mo and W-based dichalcogenides have been studied. These are semiconductors with optical properties that depend on the material thickness. Bulk TMD semiconductors possess an indirect gap, which becomes a direct one in monolayers [5,10]. Figure 1a depicts band structure calculations for  $MoS_2$  with various thicknesses [10]. Bulk  $MoS_2$  has a bandgap of 1.3 eV, with the valence band maximum at the  $\Gamma$ -point in the Brillouin zone and the conduction band minimum along the  $\Gamma$ -K direction. As the number of layers decreases, the valence band maxima and conduction band minima shift due to quantum confinement and a direct semiconductor is obtained in the monolayer limit.

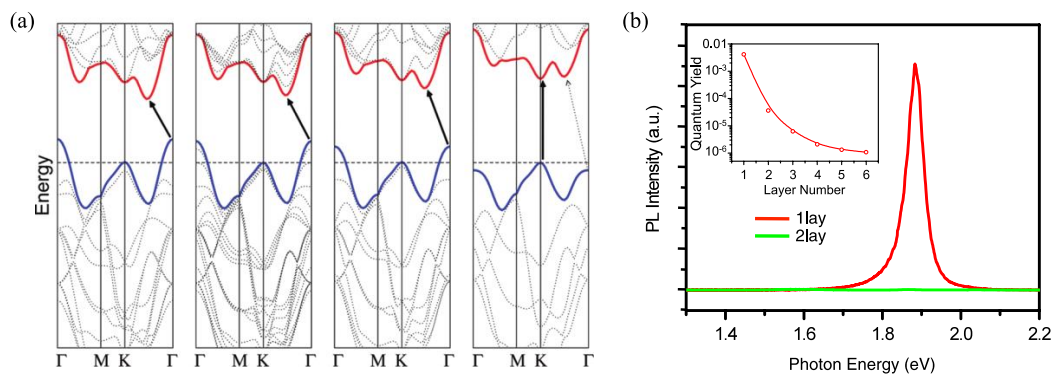


**Figure 1.** (a) Band structure calculations of bulk, four-layer, bilayer and monolayer MoS<sub>2</sub> (from left to right). Arrows indicate the lowest energy transitions. Reproduced with permission from [10], Copyright American Chemical Society, 2010. (b) Photoluminescence spectra for mono- and bilayer MoS<sub>2</sub>. Inset: Thickness-dependence of the quantum yield. Reproduced with permission from [5], Copyright American Physical Society, 2010.

The indirect-to-direct semiconductor transition is manifested as enhanced photoluminescence (PL) in monolayers. For example, in MoS<sub>2</sub>, the monolayer quantum yield is more than four orders of magnitude larger than that in bulk (see Figure 1b) [5]. Similar observations have been made for other TMDs [11]. Mo- and W-based TMDs exhibit optical bandgaps in the range  $E_X = 1.1$ – $2.0$  eV (see Table 1), *i.e.*, energies corresponding to the technologically important visible and near-infrared spectral regimes. However, despite being direct gap semiconductors, the reported photoluminescence quantum yields of as-exfoliated (or synthetically grown) TMD monolayers are poor. The room-temperature photoluminescence quantum yield of exfoliated MoS<sub>2</sub>, for example, was found to be  $4 \times 10^{-3}$  only [5]. It is believed that unintentional doping and crystal defects play a major role in suppressing the luminescence. Very recently, however, solution-based chemical treatment of MoS<sub>2</sub> by an organic superacid [12] has resulted in a quantum yield of more than 95%. Similar improvements were reported by chemical treatments of other TMDs [13]. These studies open the door for the development of more efficient TMD-based light emitters and other optoelectronic devices.

**Table 1.** Optical bandgap, spin orbit splitting and exciton binding energy for monolayer transition metal dichalcogenides (TMDs).

TMD	$E_X$ (eV)	$\Delta E_{SO,v}$ (eV)	$\Delta E_b$ (eV)
MoS <sub>2</sub>	1.85 [10]	0.16 [10]	0.57 [14]
MoSe <sub>2</sub>	1.55 [11]	0.2 [15]	0.55 [16]
WS <sub>2</sub>	2.0 [17]	0.4 [17]	0.32 [18]
WSe <sub>2</sub>	1.65 [11]	0.4 [17]	0.37 [19]
MoTe <sub>2</sub>	1.1 [20]	0.25 [20]	-

Excitons are strongly bound in 2D materials with binding energies of up to  $\sim 0.6$  eV. This is due to the enhanced electron-hole interaction in 2D systems and the reduced dielectric screening [18]. As a result, the optical spectra of TMDs are dominated by excitonic rather than band-to-band transitions even at room temperature and exhibit pronounced peaks. This is in contrast to traditional three-dimensional (3D) semiconductors, in which exciton binding energies are smaller than the thermal energy at room temperature. In TMDs, several excitonic transitions can be observed, where the two lowest-energy peaks, the A and B-excitons, arise from optical transitions between the spin-orbit split valence and conduction bands [5,10,21]. The spin-orbit splitting  $\Delta E_{SO,v}$  in the valence band varies between 0.16 and 0.4 eV (see Table 1), whereas calculations suggest a splitting  $\Delta E_{SO,c}$  in the range of tens of mV for the conduction band.

The exciton binding energies  $\Delta E_b$  of TMDs have been determined by several groups using different experimental and theoretical techniques. [14,16,18,19,22–24] The binding energy decreases with thickness due to stronger screening and also depends on strain and the dielectric environment [25]. For example, optical reflection measurements of monolayer  $WS_2$  yielded multiple resonances that can be associated with the excitonic Rydberg series (1 s, 2 s, 3 s, etc.) [18]. By fitting the resonance locations to a hydrogenic Rydberg spectrum, an exciton binding energy of 0.32 eV was determined. Similar results have been obtained for other TMDs (see Table 1). The strong confinement of excitons in TMDs leads to short radiative lifetimes, which could enable light emitters with high modulation bandwidth. In addition to neutral excitons, charged excitons, or trions (quasi-particles that are composed of two electrons and a hole, or two holes and an electron), have been studied by electrostatic control of the doping level in a field-effect transistor configuration [15,23,26]. Photoluminescence measurements demonstrated the evolution from positively charged, to neutral, and then to negatively charged excitons as the gate voltage was increased. These measurements directly revealed the trion binding energy in the range 20–40 meV, which by far exceeds that of 3D semiconductors. Energies for positively and negatively charged trions are similar due to similar effective electron and hole masses.

The band structure of a TMD monolayer exhibits two in-equivalent valleys,  $K$  and  $K'$ , located at the corners of the Brillouin zone. Because of broken inversion symmetry, spin orbit interaction splits the valence bands, giving rise to the aforementioned A and B-exciton transitions in the optical spectra. Time-reversal symmetry requires that the spin splitting is opposite in both valleys. As dictated by optical selection rules, right and left-handed circularly polarized light couples to the  $K$  and  $K'$  valleys, respectively. As a result, spin and valley degrees of freedom are coupled [27], which allows for selective valley population using circularly polarized light excitation. The valley polarization was found to remain largely preserved during the exciton lifetime [28,29]. The ability to excite, control and read-out the valley polarization could, in the future, lead to “valleytronic” devices that exploit the valley degree-of-freedom for information processing.

### 3. Photodetectors

Photodetectors convert light into electrical signals and are at the heart of many applications, such as optical communications, imaging and sensing. Compared to graphene photodetectors [30], TMD-based devices offer lower dark currents and higher photoresponsivities (the photoresponsivity  $R = I_{ph}/P_{opt}$  measures the electrical output current  $I_{ph}$  per optical input power  $P_{opt}$ ), though they work only in the near-infrared and visible spectral regimes.

Similarly to graphene, several physical mechanisms can give rise to a photoresponse in TMDs. Photoelectric [31,32] and photo-thermoelectric (Seebeck) [33] effects have been identified in devices operated under short-circuit conditions. The photoelectric effect relies on the separation of photoexcited carriers at the built-in electric field in lateral [34,35] or vertical [36,37] p-n junctions, or at the Schottky barriers at lateral TMD/metal interfaces [38], similarly to traditional photodiodes. The electric field can also be produced by application of an external voltage without driving a large dark current due to the semiconducting TMD behavior.

Optical illumination of TMD/metal interfaces can produce a photovoltage due to the different Seebeck coefficients of the metal contact and the TMD channel [33,39]. The photovoltage is defined as  $V_{PTE} = (S_1 - S_2) \Delta T_e$ , where  $S_{1,2}$  is the thermoelectric power in two differently doped regions of the TMD and  $\Delta T_e$  is the electron temperature difference between the regions. The Seebeck coefficient is related to the conductivity through the Mott formula  $S = (\pi^2 k_B^2 T / 3e) (d \ln(\sigma(E)) / dE)$ , where  $k_B$  is the Boltzmann constant,  $T$  is the temperature,  $e$  is the electron charge and  $\sigma(E)$  is the conductivity as a function of energy. The derivative has to be evaluated at the Fermi energy  $E_F$ . Large numbers for the Seebeck coefficient in  $MoS_2$ , tunable over several orders of magnitude by an external electric field, were reported by Buscema *et al.* [33]. Both photoelectric and photo-thermoelectric effects lead to moderate responsivities of the order of mA/W.

Figure 2a (inset) shows a TMD field-effect transistor structure that has been employed by several groups for MoS<sub>2</sub>-, MoSe<sub>2</sub>-, WS<sub>2</sub>-, and WSe<sub>2</sub>-based photodetection [31,32,40–45]. The same device structure has also been used in conjunction with other 2D semiconductors, such as GaSe, GaTe, In<sub>2</sub>Se<sub>3</sub>, black phosphorus and several others [46–52]. Wavelength-dependent studies have shown that the photocurrent follows the TMD absorption spectrum. It was further demonstrated that the spectral response depends on the number of TMD layers [43]. For example, MoS<sub>2</sub> mono- and bilayer devices are effective for green visible light detection, whereas three-layer MoS<sub>2</sub> is better suited for detection of red visible light. Studies have also been performed using chemical vapor deposition grown TMDs [42].

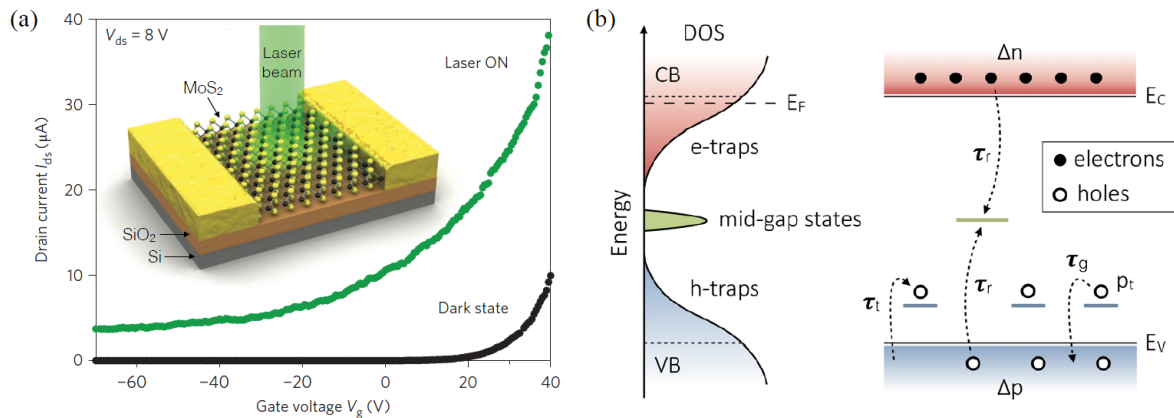


**Figure 2.** (a) Inset: Transition metal dichalcogenides TMD field-effect transistor as a photodetector. Main panel: typical gating characteristics with and without illumination. Reproduced with permission from [40], Copyright Nature Publishing Group, 2013. (b) Left: density-of-states (DOS) in MoS<sub>2</sub>. Band tail states exist underneath and above the conduction and valence band edges, respectively, that act as charge traps. Right: simplified energy band diagram that approximates the valence band tail by a discrete distribution of trap states. Reproduced with permission from [41], Copyright American Chemical Society, 2014.

By applying an external voltage, high photoresponsivities of more than 10<sup>3</sup> A/W and high photogain [40–42] have been achieved in these devices via internal amplification of the current. The photocurrent is then given as the difference between the current under optical illumination and the dark current (see Figure 2a, main panel). The term photogain refers to the fact that the number of circuit electrons generated per photoexcited carrier can be larger than one. The photogain in TMDs results from capturing of photoexcited carriers into trap states that are present either in the underlying (oxide) substrate or in the TMD itself [41]. The former is exacerbated by the high surface-to-volume ratio in 2D materials, and oxide surface treatments have been used to modify this effect [40]. The traps within the bandgap of TMDs arise from band tail states, induced by disorder or structural defects (see Figure 2b).

The trapped charge can influence the conductance of the TMD transistor (i) by shifting the threshold voltage from  $V_{th}$  in the dark to  $V_{th} - \Delta V_{th}$  under optical illumination (photogating effect), and (ii) by increasing the channel conductivity  $\Delta\sigma$  due to photo-induced excess carriers (photoconductive effect) [41,53]. The photogating effect gives rise to a photocurrent  $I_{ph} = g_m \Delta V_{th}$ , where  $g_m$  is the transistor's transconductance. The photocurrent produced by the photoconductive effect is simply given by  $I_{ph} = (W/L) V_D \Delta\sigma$ , where  $W$  and  $L$  denote the channel width and length, respectively, and  $V_D$  is the applied voltage. In general, the photoresponse is a combination of both mechanisms with the photogating effect being dominant in the transistor ON-state and the photoconductive contribution being more prominent in the OFF-state.

Responsivities and response times are typically in the range  $\sim 10^{-1}$ – $10^4$  A/W and  $\sim 10^{-4}$ – $10$  s, respectively, depending on the light intensity, the operation conditions, and the type of trap. The trap

states get filled with increasing illumination intensity, resulting in saturation of the photoresponse. It has been demonstrated that TMD encapsulation can enhance the detector performance under ambient conditions by increasing the mobility, reducing the degradation by environmental effects and preventing current fluctuations due to charge transfer into physisorbed gas molecules [54].

Photogain can also be achieved by integration of 2D materials with other materials, such as e.g., quantum dots, to realize a hybrid photodetector (see Figure 3a). This was demonstrated by sensitizing graphene with lead sulfide quantum dots [55]. Light absorption in the dots results in a charge transfer to the underlying graphene channel, which modifies the channel conductance. A related work employed the charge transfer from MoS<sub>2</sub> into graphene for photodetection [56]. Both devices, however, suffered from high dark current and large power consumption because of graphene's semi-metallic behavior. The dark current can be reduced by replacement of the graphene channel with MoS<sub>2</sub> and transistor operation in the OFF-state [57]. Light is then absorbed in the dots and the photoexcited carriers are separated at the quantum dot/MoS<sub>2</sub> interface, as shown in Figure 3b. While the holes remain trapped in the dots, electrons circulate through the MoS<sub>2</sub> channel driven by the applied voltage. The device in [57] showed a photoresponsivity of 10<sup>6</sup> A/W and a low dark current, which resulted in a detectivity of almost 10<sup>15</sup> Jones.

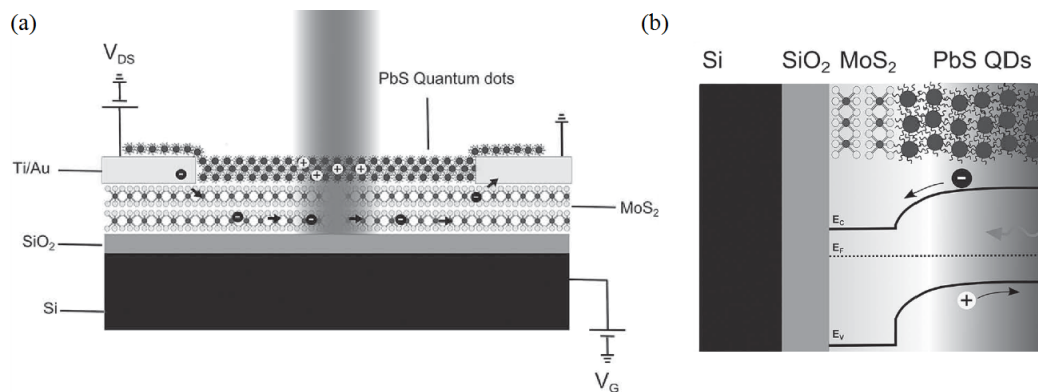


**Figure 3.** (a) Device structure of a hybrid quantum dot/MoS<sub>2</sub> photodetector. Reproduced with permission from [57], Copyright John Wiley and Sons, 2014. (b) Schematic drawing of the charge separation at the quantum dot/MoS<sub>2</sub> interface. Reproduced with permission from [57].

Two-dimensional materials can be assembled layer by layer to form a van der Waals heterostructure [58]. The surfaces of 2D materials do not have any dangling bonds and the absence of lattice matching conditions in van der Waals heterostructures permits to combine any arbitrary sequence of 2D materials. Heterostructures, comprised of vertical stacks of graphene-TMD-graphene layers, can act as photodetectors [59,60]. In these devices (see Figure 4a), graphene is employed as work function tunable electrode, whereas a TMD semiconductor is utilized as photoactive material, showing strong photon absorption. Figure 4b shows  $I$ - $V$  characteristics of a heterostack device at different back-gate voltages, which show a strong dependence on illumination. The Fermi levels in graphene can be positioned by asymmetric electrostatic or chemical doping of the top and bottom graphene sheets, so that a built-in electric field is produced even without bias (see Figure 4c). The field can further be enhanced by application of an external voltage. Upon illumination, photo-generated carriers are separated in the TMD layer and collected by the graphene electrodes. The photocurrent was mapped by scanning photocurrent measurements and it was verified that the photocurrent was indeed generated across the whole face of the heterojunction. Samples were also prepared on flexible substrates. The measured responsivities were of the order of  $\sim 0.1$  A/W, comparable to state-of-the-art bulk semiconductor flexible membranes [61]. Despite the low out-of-plane mobility in layered TMDs [62], picosecond photoresponse times were measured because of the short carrier travel distance in ultrathin heterostructures [63].

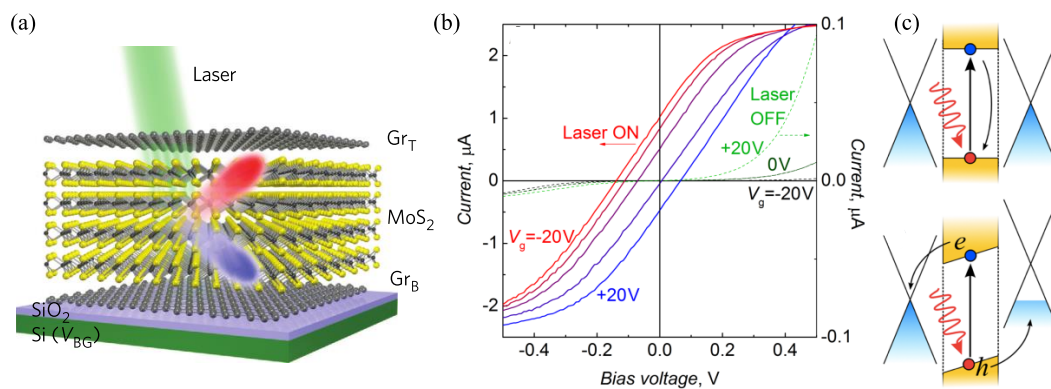


**Figure 4.** (a) Schematic drawing of a graphene-TMD-graphene photodetector. Reproduced with permission from [59], Copyright Nature Publishing Group, 2013. (b) Electrical characteristics with and without optical illumination. Reproduced with permission from [60], Copyright The American Association for the Advancement of Science, 2013. (c) Schematic band diagrams for symmetric graphene doping (upper image; no photoresponse without bias) and asymmetric doping (lower image; charge separation due to built-in electric field). Reproduced with permission from [60].

#### 4. Light-Emitters

Electroluminescence (EL)—the emission of light from an electronic device in response to an electric current—results from radiative recombination of charge carriers (electron-hole pairs or excitons) in a semiconductor. It forms the basis of light emitting optoelectronic devices like light-emitting diodes (LEDs) or semiconductor lasers. Monolayer TMDs are usually used for EL-devices because of their direct band gap. Light emission from multi-layer TMDs was reported by carrier redistribution from the indirect to the direct valleys in a high electric field [64], by filling the indirect valleys in the conduction and valence bands in an electric-double-layer transistor [65], or by the injection of hot electrons from metal/TMD junction [66].

Sundaram *et al.* [67] exploited hot carrier processes by driving a high unipolar current through a monolayer MoS<sub>2</sub> field-effect transistor to achieve electroluminescence. A high drain-source bias leads to strong band bending in the vicinity of the metal contacts of the device. Electrons, which are injected from the metal to the semiconductor channel, are accelerated by the electric field and can eventually gain enough kinetic energy to create electron-hole pairs by impact excitation. Due to a large exciton binding energy in 2D materials (which also prevents the bound electron-hole pairs from being dissociated by the electric field), impact excitation is very efficient in low-dimensional systems [68,69]. The characteristic features of impact excitation include a threshold behavior and an exponential increase of the emission above threshold [68]. The localization of the light emission near the metal contact, where the electric field is the highest, was confirmed by spatial mapping.

An electroluminescence efficiency of  $10^{-5}$  at wavelengths in accordance with the A-excitonic peak of MoS<sub>2</sub> was achieved. Ponomarev *et al.* [70] demonstrated electroluminescence emission from MoS<sub>2</sub> grown by chemical vapor deposition (CVD). Transport in the space-charge limited regime and the existence of a large number of deep traps that act as localization centers, led to emission from an area close to the injecting contact at low source-drain bias in their device.

Light emitting diodes usually rely on the recombination of electrons and holes in a p-n junction. Both types of carriers are injected into a channel where they recombine radiatively. This emission process does not have a threshold and is more efficient than electron-hole pair generation by impact excitation. Typically, two regions of a semiconductor are treated with different doping atoms. Choi *et al.* [71] showed chemical p-type doping of intrinsically n-type few-layer MoS<sub>2</sub> using AuCl<sub>3</sub> and demonstrated current rectification in their device, but light emission from chemically doped p-n junctions has not yet been demonstrated.

Pospischil *et al.* [34], Baugher *et al.* [35] and Ross *et al.* [72] demonstrated the first monolayer TMD p-n junctions, formed by electrostatic doping. In their devices two gate electrodes couple to different regions of a TMD crystal, as illustrated in Figure 5a. Biasing of one gate electrode with a positive voltage and the other gate electrode with a negative voltage leads to injection of electrons and holes into the channel. Efficient electron and hole transport was accomplished by two different metal contacts (Ti/Au, Pd/Au) fabricated on a monolayer of WSe<sub>2</sub>. By driving a forward current through the p-n junction, electroluminescence emission was achieved at comparable wavelengths as the emission of the neutral exciton (~750 nm). This suggests that electrons and holes form excitons before radiative recombination. The electroluminescence efficiency in such devices is ~0.1%, limited by resistive losses at the contacts and non-radiative recombination. Electroluminescence from WS<sub>2</sub> was achieved by using ionic liquid gating, yielding visible light emission at ~630 nm [73].

Vertical structures—with current flowing perpendicular to the layers—overcome several problems that arise in their lateral counterparts. The contact resistance is reduced due to a larger contact area and the emission is enhanced due to higher current density. Moreover, the whole device area can contribute to light emission, which allows for easier scalability. Two types of vertical structures can be distinguished: First, a 2D material can be placed on top of a 3D semiconductor (2D/3D heterostack), and second, several different 2D materials can be stacked on top of each other (2D/2D heterostack). In both cases, van der Waals forces between the layers are high enough to keep the stack together.

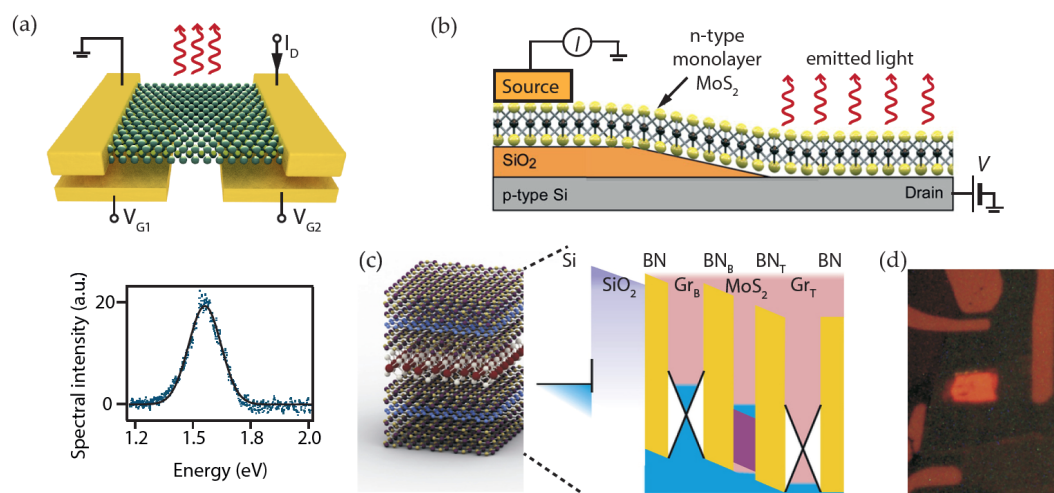


**Figure 5.** Light emitting devices. (a) Lateral device design (top). Split-gate electrodes couple to two different regions of a WSe<sub>2</sub> monolayer to efficiently inject electrons and holes into the channel. The bottom panel shows electroluminescence response under a forward bias current of 200 nA. Reproduced with permission from [34], Copyright Nature Publishing Group, 2014. (b) 3D/2D heterojunction. A p-n junction is formed between p-doped bulk silicon and n-doped monolayer MoS<sub>2</sub>. Light emission occurs at the whole junction area. Reproduced with permission from [74], Copyright American Chemical Society, 2014. (c) Schematic of a Si/SiO<sub>2</sub>/BN/Gr/BN/MoS<sub>2</sub>/BN/Gr/BN heterostack light-emitting diode (Gr, graphene; BN, hexagonal boron nitride) and corresponding band diagram under forward bias. Reproduced with permission from [75], Copyright Nature Publishing Group, 2015. (d) Optical microscope image of the emission of the device described in (c). Reproduced with permission from [75].

Three-dimensional/two-dimensional heterojunctions (illustrated in Figure 5b) have been shown by Ye *et al.* [76] and Lopez-Sanchez *et al.* [74]. They placed a monolayer MoS<sub>2</sub> sheet on a silicon wafer, where the p-doped silicon acts as hole-injector, while electrons are injected from the intrinsically n-doped MoS<sub>2</sub> sheet. Light emission occurred from the entire device area [74]. Emission spectra showed contributions from neutral, charged and bound excitonic species, depending on current density and temperature. Li *et al.* [64] demonstrated light emission from a few-layer MoS<sub>2</sub>/GaN heterostructures.

Two-dimensional/two-dimensional heterostructures can be composed of mono- or few-layer sheets of metallic (e.g., graphene), insulating (e.g., hexagonal boron nitride, hBN) or semiconducting (e.g., MoS<sub>2</sub> or WSe<sub>2</sub>) crystals. Different composition allows for different emission wavelengths, tailored to the need of the application. Graphene is widely used as a transparent electrode on top and bottom to inject electrons and holes into the TMD layer (Figure 5c). Thin hBN layers between the electrode and the semiconductor prevent carriers from direct tunneling between the graphene sheets and allow for accumulation of carriers in the semiconductor. Electroluminescence sets in above a threshold that is associated with the alignment of the top and bottom graphene Fermi levels with the TMD conduction and valence band, respectively. Withers *et al.* [75] could achieve external quantum efficiencies (EQEs) higher than 1% at room temperature, a tenfold increase compared to the lateral p-n junctions. By using multiple quantum well structures, EQEs of up to 8.4% were obtained at low temperatures. In another study, the same group demonstrated light emission from a monolayer WSe<sub>2</sub> sheet with enhanced brightness at room temperature (EQE 5%) [77]. This counter-intuitive behavior was explained by a giant conduction band splitting ( $\sim 30$  meV) with opposite spin orientations for the lowest energy transition in tungsten based TMDs, resulting in a highly efficient dark (non-radiative) excitonic recombination channel at low temperatures [21]. Heterostacks are flexible due to the atomically thickness of the used materials, which enables flexible and semi-transparent optoelectronics.

Spontaneous emission from a TMD monolayer can be enhanced due to the Purcell effect by coupling to an optical cavity [78,79]. Enhanced PL emission from MoS<sub>2</sub>, placed on top of a microdisc cavity, was shown by Reed *et al.* [80] Photonic crystal cavities [81] (Figure 6a) or microdisc cavities [82,83] (Figure 6b) with even higher quality factors have been used to demonstrate lasing. These studies show that an optically pumped TMD monolayer can provide sufficient optical gain to compensate for the cavity losses. All three devices demonstrated ultra-low lasing threshold and continuous-wave operation with optical pump power as low as 27 nW at 130 K [81]. Typical characteristics of a laser—abrupt change in the slope of the output light intensity and emission linewidth—were observed, but photon statistic measurements yet need to be carried out to get deeper insight into the lasing behavior.

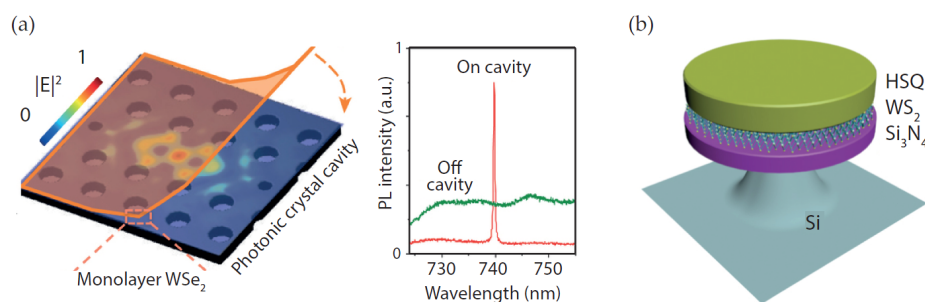


**Figure 6.** (a) Photonic crystal cavity WSe<sub>2</sub> nanolaser. The color profile shows the fundamental cavity mode before a WSe<sub>2</sub> monolayer is transferred on the structure. The on-cavity excitation photoluminescence spectrum (red) shows a narrow emission line compared to off-cavity excitation (green). Reproduced with permission from [81], Copyright Nature Publishing Group, 2015. (b) Schematic image of a WS<sub>2</sub> microdisc laser. Sandwiching the WS<sub>2</sub> monolayer between silicon nitride and hydrogen silsesquioxane (HSQ) ensures a higher confinement factor. Reproduced with permission from [83], Copyright Nature Publishing Group, 2015.

## 5. Single Photon Emitters

In quantum technologies (*i.e.*, quantum communications and quantum computing), single-photon sources are a basic building block. Single molecules, quantum dots or color centers in diamond are traditionally used for the generation of single-photons. In TMDs, bright and narrow lines in the PL spectrum are observed at crystal imperfections, mostly at the flake-edge or the transition from mono- to few-layer flakes (compare Figure 7a,b). These structural defects and/or local strain are possibly

the origin of the narrow-line emission. Studies performed by several groups [84–88] confirmed single photon emission from defect centers by photon antibunching measurements (Figure 7c). Second-order autocorrelation factors  $g^{(2)}(0)$  in the range between 0.14 and 0.36 were determined. Due to charge confinement and strong coupling between charge carriers and phonons, quantum emission was observed only at low temperatures. The emission linewidth was determined to be about 100–120  $\mu\text{eV}$  for freestanding [84] and supported samples [85–88]. Luminescence decay times were measured to be in the range of a few ns, comparable to the decay time of the free exciton at room temperature ( $\sim 4$  ns) [89].

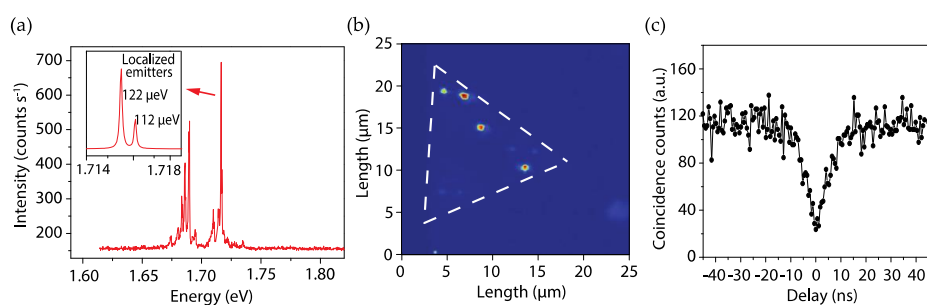


**Figure 7.** (a) Photoluminescence (PL) spectrum of localized emitters showing narrow emission lines. The inset shows a high-resolution spectrum of the brightest line in the main panel. (b) PL intensity map of the narrow emission lines centered around 1.719 eV. The dashed line indicates the monolayer. (c) Second order correlation measurement of the PL of a localized emitter showing photon antibunching. (a–c) reproduced with permission from [86], Copyright Nature Publishing Group, 2015.

All studies confirm long-term stability of the defect centers and robustness against temperature cycling as well as exposure to ambient (air) conditions. Temporal stability of the spectral position (jittering) was found to be on the order of the linewidth ( $\sim 1$  meV) on a millisecond timescale and larger jumps occurred on a longer timescale [87]. Stability improved for low excitation power and freshly exfoliated samples. Jittering may be reduced by encapsulation of the TMD sheets in dielectric coatings like thin flakes of hBN.

Tonndorf *et al.* [84] found that single photon emission centers can be introduced artificially by mechanical scratching. An external electric field can be used to control the emission of localized defect centers, while a magnetic field allows for spectral manipulation [87,88]. Electrically driven single-photon emission, which would allow for convenient and compact sources, is yet to be demonstrated.

Quantum emission from mono- and multi-layer hexagonal boron nitride (hBN) with high emission rates at room temperature was demonstrated by Tran *et al.* [90]. Calculations confirmed that anti-site nitrogen vacancies are responsible for single-photon emission with an energy within the bandgap of hBN.

## 6. Photovoltaics

Photovoltaic cells are used to convert solar energy into electricity. Solar cells that rely on inorganic or organic semiconductors have been developed over the last decades. Recently, TMDs are reconsidered as alternative for photovoltaics because of their band gap in the visible part of the electromagnetic spectrum and strong optical absorption [91]. Moreover, TMDs are interesting from a technological point of view, as they are chemically stable, environmentally sustainable and can potentially be produced at low cost. Calculations of graphene/MoS<sub>2</sub> [92] and WS<sub>2</sub>/MoS<sub>2</sub> [93] monolayer heterojunction solar cells predict a maximum power conversion efficiency of  $\sim 1\%$ , limited by the, in absolute numbers, low optical absorption of the atomically thin materials. Absorption enhancement is therefore necessary and can be achieved by stacking of 2D materials, using few-layer sheets or exploiting plasmonic effects [94].

The photovoltaic properties of various bulk and thin film TMD crystals have been studied since the 1980s [95]. Following the demonstration of monolayer graphene and TMD crystals, photovoltaic

properties of ultrathin layers have been investigated. An electrostatically induced p-n junction diode device (compare the device in Figure 5a) shows photovoltaic response when operated in diode configuration [34,35]. Power conversion efficiency  $\eta = P_{in}/P_{el}$  ( $P_{in}$  incident light power;  $P_{el}$ , electrical output power) of the solar cells was found to be on the order of 0.5% limited by the low absorption in the monolayer and recombination of charge carriers. In a similar device structure, Memaran *et al.* [96] demonstrated  $\eta > 14\%$  and fill factors of  $\sim 70\%$  at AM-1.5 spectral irradiation, using multi-layer MoSe<sub>2</sub>. Similar results were obtained by other groups [97] and for a MoS<sub>2</sub>/black phosphorus solar cell [98].

Schottky junctions can also create lateral electric fields. Fontana *et al.* [38] studied MoS<sub>2</sub> field-effect devices with two different contact metals. Due to different work functions in gold and palladium, photogenerated electron-hole pairs are separated by the built-in field at the contact region and a give rise to a photovoltaic effect.

Lateral electrode arrangement prevents easy scalability of TMD photovoltaic cells, and it is therefore desirable to fabricate vertical junctions. Stacking single or few-layer sheets of TMD crystals on top of each other results in p-n junction heterostacks, held together by van der Waals forces.

A photovoltaic response in such devices was reported by Furchi *et al.* [36], Lee *et al.* [37], Flöry *et al.* [99] and Cheng *et al.* [100]. The device forms a p-n junction at the interface between two TMD monolayers (*i.e.*, MoS<sub>2</sub> and WSe<sub>2</sub>), as depicted in Figure 8a. Due to different electron affinities of both materials, a type-II heterojunction is formed, meaning that the lowest energy electron and highest energy hole states are located in the MoS<sub>2</sub> and WSe<sub>2</sub> layers, respectively. Electrical measurements, while increasing the illumination power from 180 W/m<sup>2</sup> to 6400 W/m<sup>2</sup>, showed the shift of the  $I$ - $V$  curve, and a maximum electrical power of  $P_{el} \sim 15$  pW was extracted from the solar cell (depicted in the main panel and inset of Figure 8b). As the doping concentration in the monolayer sheets is determined by extrinsic factors, a gate voltage is needed to tune the stack to a regime in which a vertical p-n junction is formed. Charge transfer between individual TMD sheets was found to be ultrafast (<100 fs) and highly efficient (almost 100%) [36,37,101–103].

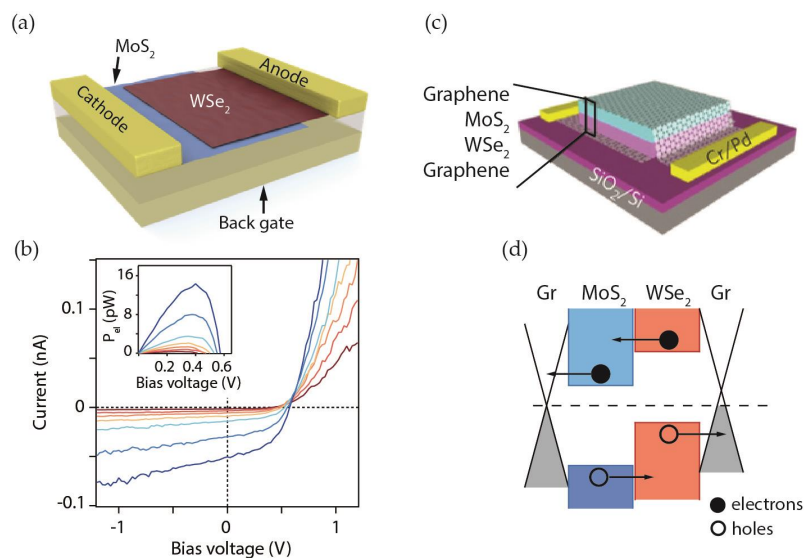


**Figure 8.** Photovoltaic cells. (a) Schematic device layout of a vertical heterojunction device with lateral contacts. A p-n junction is formed at the interface between an n-doped MoS<sub>2</sub> sheet and a p-doped WSe<sub>2</sub> sheet. Reproduced with permission from [36], Copyright Nature Publishing Group, 2014. (b) Electrical (main panel) and optical (inset) characteristics of the solar cell. The incident laser power is increased from 180 W/m<sup>2</sup> (red curve) to 6400 W/m<sup>2</sup> (blue curve). Reproduced with permission from [36]. (c) Schematic device layout of a vertical heterojunction with graphene electrodes on bottom and top, which allow for vertical carrier extraction. Reproduced with permission from [37], Copyright Nature Publishing Group, 2014. (d) Schematic of the bandstructure. The horizontal arrows indicate exciton dissociation and charge carrier diffusion. Reproduced with permission from [37].

Under bias, a diode-like rectification behavior was observed, although the origin of rectification is different from the mechanism in a traditional 3D semiconductor diode. A forward bias voltage drives electrons (holes) in MoS<sub>2</sub> (WSe<sub>2</sub>) to the area of the heterojunction, where they either recombine or overcome the conduction (valence) band offsets to be injected into the other layer and diffuse towards the contacts. In an ideal diode, diffusion dominates over recombination, but it was found that in atomically thin p-n junctions recombination plays a substantial role [36]. The lack of a depletion region in vertical heterojunctions implies that majority carriers in the individual layers are in close proximity to each other, which results in strong interlayer recombination [36,100].

The photovoltaic response of such vertical devices under white light illumination can be explained as follows: Absorption of photons creates electron-hole pairs (excitons) in both layers, which then relax to minimum energy, driven by the type-II band offset. Subsequently, the relaxed charge carriers diffuse towards the contacts, resulting in a photocurrent. During this diffusion process, interlayer recombination occurs that reduces the efficiency of the solar cell. Measurements show an efficiency and a fill factor of ~0.2% and ~50%, respectively, for such heterostructures [36]. Scalability can be achieved by vertical contacts using graphene as electrode material, as schematically depicted in Figure 8c. A schematic band diagram is shown in Figure 8d. Electrodes on the top and bottom of the p-n junction allow for vertical carrier extraction and also increase the overall efficiency of the cell. Lee *et al.* [37] report multilayer heterojunctions, which, compared to their monolayer counterparts, show about an order of magnitude higher EQE. Due to the thickness-dependent competition between generation, collection and recombination of charge carriers, further optimization of the layer thickness probably leads to even higher efficiencies.

Vertical p-n junction devices using other material combinations, such as GaTe/MoS<sub>2</sub> [104] and organohalide perovskite/WSe<sub>2</sub> [105], the formation of a p-n junction by surface charge induced doping [106], as well as organic/inorganic material junctions [107–109] have been demonstrated and gave similar results.

## 7. Valleytronics

Electron spin is probably the most studied quantum degree of freedom in condensed matter physics. Excitonic transitions in TMDs are not only associated with the spin degree of freedom but also with the valley degree of freedom [110]. Valley degree of freedom is a result of degenerate energy extrema in momentum space, as the  $K$  and  $K'$  valleys in 2D materials are related to each other by time reversal. To uncover and manipulate the valley degree of freedom, all-optical methods were exploited by several groups, and it was found that the valley polarization is robust and preserved during hot-carrier relaxation, exciton formation and radiative recombination processes [27,28,111–113]. On the other hand, only a few studies on electro-optical valley-dependent devices have been published.

Charge carriers in the  $K$  and  $K'$  valleys experience effective magnetic fields with opposite signs, which allow for the generation of valley-polarization by circularly polarized optical pumping, due to the broken inversion symmetry in TMD monolayers [110]. Therefore, carriers in the according valleys experience opposite Lorentz-like forces and are deflected in opposite directions perpendicular to the current flow. In analogy to the spin Hall effect, this phenomenon is called the valley Hall effect. Mak *et al.* [114] measured the photovoltage, which was produced by circularly polarized light in a MoS<sub>2</sub> Hall bar device (Figure 9a). The sign of the Hall voltage could be controlled by the helicity of the light, whereas there was no effect detectable for linearly polarized light or (inversion-symmetric) bilayer devices. Other studies demonstrated a valley dependent photodetector in CVD grown MoS<sub>2</sub> [115] and the generation of spin-valley-coupled circular photogalvanic currents in WSe<sub>2</sub> [116].

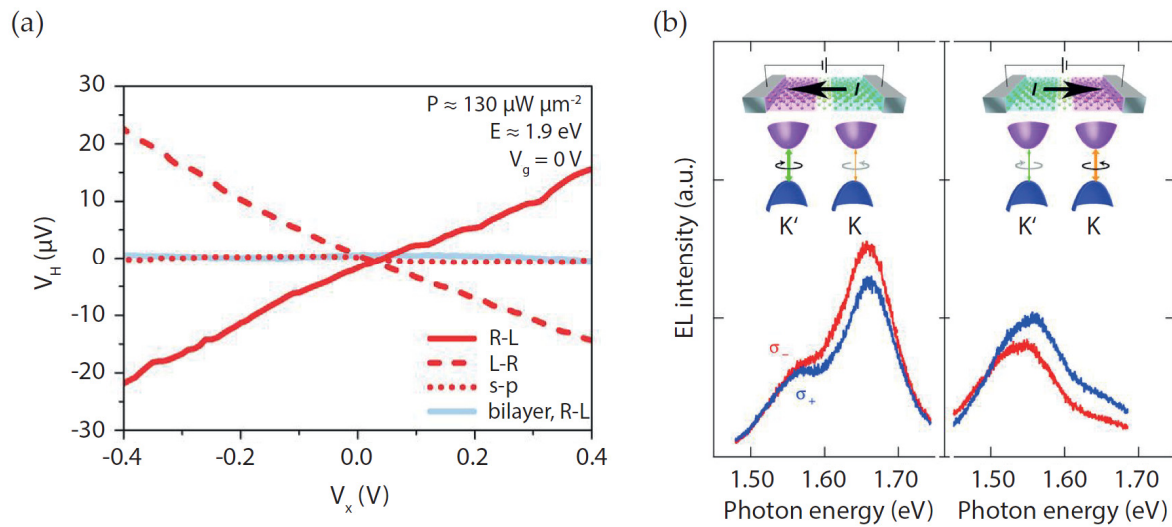


**Figure 9.** (a) Source drain bias dependence ( $V_x$ ) of the Hall voltage ( $V_H$ ) for a monolayer MoS<sub>2</sub> device for different light polarizations demonstrating the valley Hall effect. Reproduced with permission from [114], Copyright The American Association for the Advancement of Science, 2014. (b) Lateral p-n diode with opposite current flow direction (top) and corresponding dominant excitonic emission (bottom), representing the contribution to electroluminescence from  $K$  and  $K'$  valleys. Reproduced with permission from [65], Copyright The American Association for the Advancement of Science, 2014.

Zhang *et al.* [65] fabricated a chiral light-emitting transistor by forming a multi-layer WSe<sub>2</sub> p-n junction using electric double layer gating. As a result of the high carrier density induced by ionic liquid gating, they were able to populate the direct gap  $K$  and  $K'$  valleys and achieve light emission. The strong gate field breaks the inversion symmetry in the multi-layer TMD and recovers the valley circular dichroism that is otherwise only present in monolayers. The electroluminescence from their device was found to be circularly polarized, with the direction of the polarization depending on the direction of the current flow. If the device was operated in ambipolar mode and current was driven from right to left, the left-handed circular polarized light emission ( $\sigma^-$ ) dominated over the right-handed emission ( $\sigma^+$ ) as shown in the left panel in Figure 9b. On the other hand, by changing the direction of the current, the  $\sigma^+$  polarization dominated over  $\sigma^-$  polarization (right panel in Figure 9b). The degree of circular polarization reached values up to 45%, which is comparable to PL from TMD monolayers.

## 8. Conclusions

We finally compare the performance of TMD optoelectronic devices with today's technologies and discuss potential future applications and remaining challenges.

Many applications in optoelectronics (photovoltaic solar cells, display panels, *etc.*) require large-area dimensions for which traditional semiconductors—especially III-Vs—are too costly. Alternative technologies, such as e.g., organic semiconductors, are thus currently employed, but these exhibit rather low material quality and suffer from degradation issues. TMDs, on the other hand, are crystals with high material quality and stability. In addition, they are bendable, thus providing opportunities for novel applications, such as wearable devices. The prospects for commercialization will depend on device reliability and means for low-cost and large-volume production. The growth of TMD monolayers has made large progress in recent years [117–126], but routes to control the chemical doping are still to be devised. Direct growth on plastic substrates does not seem feasible. Therefore, techniques need to be developed to transfer TMDs from the growth substrate to a target substrate on an industrial scale [124]. Besides the aforementioned technological advantages, TMDs also offer new physics. The large exciton binding energy could be exploited for devices that allow the

controlled generation and manipulation of excitons at room temperature. The short radiative lifetime of excitons provides the opportunity for high-speed modulation of TMD-based light sources for data communications. The ability to generate, control and read-out valley polarizations in monolayer TMDs, may lead to devices for quantum computation with valley-qubits. Moreover, the endless number of possibilities of stacking different 2D materials into van der Waals heterostructures could allow for the realization of materials with tailored properties and functionalities.

Already today, TMD photodetectors exhibit photoresponsivities that are comparable to that of state-of-the-art 3D semiconductor devices. In addition, the integration into multi-pixel arrays seems feasible. The lack of a killer application, however, is an issue. Because of their rather large bandgap, TMDs work mainly in the visible spectral regime, which is well covered by the highly mature Si technology. In the infrared, hybrid devices that combine TMDs with other materials (e.g., quantum dots) could offer a low-cost alternative to micro-bolometers for imaging.

Research on TMD light-emitters has made large progress recently. Efficiencies are comparable to that of state-of-the-art organic light-emitting diodes. Among all TMDs studied so far, WS<sub>2</sub> has the largest bandgap and emits red visible light. For full-color displays, green and blue visible light emission would additionally be required. Given the large exciton binding energies in TMDs, it might be possible to shift the emission to somewhat shorter wavelengths (e.g., by engineering of the dielectric environment), but achieving blue light emission does not seem feasible. Other 2D semiconductors, that possess larger bandgaps, may eventually allow overcoming this limitation. The optical semi-transparency of such displays might find application in augmented reality and related applications.

First experiments on TMD-based photovoltaics are encouraging. The dissociation of excitons into free carriers seems to be efficient, despite the large exciton binding energies. At present, the most promising device concept is the graphene/p-TMD/n-TMD/graphene vertical junction. A major challenge that remains is the scaling of micrometer-sized proof-of-principle devices to macroscopic dimensions. This will require extending the growth of van der Waals heterostructures to large areas [100,127].

**Acknowledgments:** Funding by the Austrian Science Fund FWF (START Y 539-N16) and the European Union Seventh Framework Programme (grant agreement No. 604391 Graphene Flagship) is acknowledged.

**Author Contributions:** Both authors contributed to performing the literature review and writing the manuscript.

**Conflicts of Interest:** The authors declare no conflict of interest.

## References

1. Novoselov, K.S.; Geim, A.K.; Morozov, S.V.; Jiang, D.; Zhang, Y.; Dubonos, S.V.; Grigorieva, I.V.; Firsov, A.A. Electric field effect in atomically thin carbon films. *Science* **2004**, *306*, 666–669. [[CrossRef](#)] [[PubMed](#)]
2. Novoselov, K.S.; Jiang, D.; Schedin, F.; Booth, T.J.; Khotkevich, V.V.; Morozov, S.V.; Geim, A.K. Two-dimensional atomic crystals. *Proc. Natl. Acad. Sci. USA* **2005**, *102*, 10451–10453. [[CrossRef](#)] [[PubMed](#)]
3. Frindt, R.F.; Yoffe, A.D. Physical properties of layer structures: Optical properties and photoconductivity of thin crystals of molybdenum disulphide. *Proc. R. Soc. A* **1963**, *273*, 69–83. [[CrossRef](#)]
4. Wilson, J.A.; Yoffe, A.D. Transition metal dichalcogenides: Discussion and interpretation of observed optical, electrical and structural properties. *Adv. Phys.* **1969**, *18*, 193–335. [[CrossRef](#)]
5. Mak, K.F.; Lee, C.; Hone, J.; Shan, J.; Heinz, T.F. Atomically thin MoS<sub>2</sub>: A new direct-gap semiconductor. *Phys. Rev. Lett.* **2010**, *105*. [[CrossRef](#)] [[PubMed](#)]
6. Radisavljevic, B.; Radenovic, A.; Brivio, J.; Giacometti, V.; Kis, A. Single-layer MoS<sub>2</sub> transistors. *Nat. Nanotechnol.* **2011**, *6*, 147–150. [[CrossRef](#)] [[PubMed](#)]
7. Wang, Q.H.; Kalantar-Zadeh, K.; Kis, A.; Coleman, J.N.; Strano, M.S. Electronics and optoelectronics of two-dimensional transition metal dichalcogenides. *Nat. Nanotechnol.* **2012**, *7*, 699–712. [[CrossRef](#)] [[PubMed](#)]
8. Chhowalla, M.; Shin, H.S.; Eda, G.; Li, L.-J.; Loh, K.P.; Zhang, H. The chemistry of two-dimensional layered transition metal dichalcogenide nanosheets. *Nat. Chem.* **2013**, *5*, 263–275. [[CrossRef](#)] [[PubMed](#)]

9. Jariwala, D.; Sangwan, V.K.; Lauhon, L.J.; Marks, T.J.; Hersam, M.C. Emerging device applications for semiconducting two-dimensional transition metal dichalcogenides. *ACS Nano* **2014**, *8*, 1102–1120. [[CrossRef](#)] [[PubMed](#)]
10. Splendiani, A.; Sun, L.; Zhang, Y.; Li, T.; Kim, J.; Chim, C.-Y.; Galli, G.; Wang, F. Emerging photoluminescence in monolayer MoS<sub>2</sub>. *Nano Lett.* **2010**, *10*, 1271–1275. [[CrossRef](#)] [[PubMed](#)]
11. Tonndorf, P.; Schmidt, R.; Böttger, P.; Zhang, X.; Börner, J.; Liebig, A.; Albrecht, M.; Kloc, C.; Gordan, O.; Zahn, D.R.T.; *et al.* Photoluminescence emission and Raman response of monolayer MoS<sub>2</sub>, MoSe<sub>2</sub>, and WSe<sub>2</sub>. *Opt. Express* **2013**, *21*, 4908–4916. [[CrossRef](#)] [[PubMed](#)]
12. Amani, M.; Lien, D.-H.; Kiriya, D.; Xiao, J.; Azcatl, A.; Noh, J.; Madhvapathy, S.R.; Addou, R.; KC, S.; Dubey, M.; *et al.* Near-unity photoluminescence quantum yield in MoS<sub>2</sub>. *Science* **2015**, *350*, 1065–1068. [[CrossRef](#)] [[PubMed](#)]
13. Han, H.V.; Lu, A.-Y.; Lu, L.-S.; Huang, J.-K.; Li, H.; Hsu, C.-L.; Lin, Y.-C.; Chiu, M.-H.; Suenaga, K.; Chu, C.-W.; *et al.* Photoluminescence enhancement and structure repairing of monolayer MoSe<sub>2</sub> by hydrohalic acid treatment. *ACS Nano* **2016**, *10*, 1454–1461. [[CrossRef](#)] [[PubMed](#)]
14. Klots, A.R.; Newaz, A.K.M.; Wang, B.; Prasai, D.; HKrzyzanowska, H.; Lin, J.; Caudel, D.; Ghimire, N.J.; Yan, J.; Ivanov, B.L.; *et al.* Probing excitonic states in suspended two-dimensional semiconductors by photocurrent spectroscopy. *Sci. Rep.* **2014**, *4*. [[CrossRef](#)] [[PubMed](#)]
15. Ross, J.S.; Wu, S.; Yu, H.; Ghimire, N.J.; Jones, A.M.; Aivazian, G.; Yan, J.; Mandrus, D.G.; Xiao, D.; Yao, W.; *et al.* Electrical control of neutral and charged excitons in a monolayer semiconductor. *Nat. Commun.* **2013**, *4*. [[CrossRef](#)] [[PubMed](#)]
16. Ugeda, M.M.; Bradley, A.J.; Shi, S.-F.; da Jornada, F.H.; Zhang, Y.; Qiu, D.Y.; Ruan, W.; Mo, S.-K.; Hussain, Z.; Shen, Z.-X.; *et al.* Giant bandgap renormalization and excitonic effects in a monolayer transition metal dichalcogenide semiconductor. *Nat. Mater.* **2014**, *13*, 1091–1095. [[CrossRef](#)] [[PubMed](#)]
17. Zhao, W.; Ghorannevis, Z.; Chu, L.; Toh, M.; Kloc, C.; Tan, P.-H.; Eda, G. Evolution of electronic structure in atomically thin sheets of WS<sub>2</sub> and WSe<sub>2</sub>. *ACS Nano* **2013**, *7*, 791–797. [[CrossRef](#)] [[PubMed](#)]
18. Chernikov, A.; Berkelbach, T.C.; Hill, H.M.; Rigosi, A.; Li, Y.; Aslan, O.B.; Reichman, D.R.; Hybertsen, M.S.; Heinz, T.F. Exciton binding energy and nonhydrogenic rydberg series in monolayer WS<sub>2</sub>. *Phys. Rev. Lett.* **2014**, *113*. [[CrossRef](#)]
19. He, K.; Kumar, N.; Zhao, L.; Wang, Z.; Mak, K.F.; Zhao, H.; Shan, J. Tightly bound excitons in monolayer WSe<sub>2</sub>. *Phys. Rev. Lett.* **2014**, *113*. [[CrossRef](#)] [[PubMed](#)]
20. Ruppert, C.; Aslan, O.B.; Heinz, T.F. Optical properties and band gap of single- and few-layer MoTe<sub>2</sub> crystals. *Nano Lett.* **2014**, *14*, 6231–6236. [[CrossRef](#)] [[PubMed](#)]
21. Kormányos, A.; Burkard, G.; Gmitra, M.; Fabian, J.; Zólyomi, V.; Drummond, N.D.; Fal'ko, V. k.p theory for two-dimensional transition metal dichalcogenide semiconductors. *2D Mater.* **2015**, *2*. [[CrossRef](#)]
22. Ramasubramaniam, A. Large excitonic effects in mono-layers of molybdenum and tungsten dichalcogenides. *Phys. Rev. B* **2012**, *86*. [[CrossRef](#)]
23. Berkelbach, T.C.; Hybertsen, M.S.; Reichman, D.R. Theory of neutral and charged excitons in monolayer transition metal dichalcogenides. *Phys. Rev. B* **2013**, *88*. [[CrossRef](#)]
24. Qiu, D.Y.; da Jornada, F.H.; Louie, S.G. Optical spectrum of MoS<sub>2</sub>: Many-body effects and diversity of exciton states. *Phys. Rev. Lett.* **2013**, *111*. [[CrossRef](#)] [[PubMed](#)]
25. Castellanos-Gomez, A.; Roldán, R.; Cappelluti, E.; Buscema, M.; Guinea, F.; van der Zant, H.S.J.; Steele, G.A. Local strain engineering in atomically thin MoS<sub>2</sub>. *Nano Lett.* **2013**, *13*, 5361–5366. [[CrossRef](#)] [[PubMed](#)]
26. Mak, K.F.; He, K.; Lee, C.; Lee, G.H.; Hone, J.; Heinz, T.F.; Shan, J.S. Tightly bound triions in monolayer MoS<sub>2</sub>. *Nat. Mater.* **2013**, *12*, 207–211. [[CrossRef](#)] [[PubMed](#)]
27. Xiao, D.; Liu, G.-B.; Feng, W.; Xu, X.; Yao, W. Coupled spin and valley physics in monolayers of MoS<sub>2</sub> and other group-VI dichalcogenides. *Phys. Rev. Lett.* **2012**, *108*. [[CrossRef](#)] [[PubMed](#)]
28. Mak, K.F.; He, K.; Shan, J.; Heinz, T.F. Control of valley polarization in monolayer MoS<sub>2</sub> by optical helicity. *Nat. Nanotechnol.* **2012**, *7*, 494–498. [[CrossRef](#)] [[PubMed](#)]
29. Jones, A.M.; Yu, H.; Ghimire, N.J.; Wu, S.; Aivazian, G.; Ross, J.S.; Zhao, B.; Yan, J.; Mandrus, D.G.; Xiao, D.; *et al.* Optical generation of excitonic valley coherence in monolayer WSe<sub>2</sub>. *Nat. Nanotechnol.* **2013**, *8*, 634–638. [[CrossRef](#)] [[PubMed](#)]

30. Koppens, F.H.L.; Mueller, T.; Avouris, Ph.; Ferrari, A.C.; Vitiello, M.S.; Polini, M. Photodetectors based on graphene, other two-dimensional materials and hybrid systems. *Nat. Nanotechnol.* **2014**, *9*, 780–793. [[CrossRef](#)] [[PubMed](#)]
31. Yin, Z.; Li, H.; Li, H.; Jiang, L.; Shi, Y.; Sun, Y.; Lu, G.; Zhang, Q.; Chen, X.; Zhang, H. Single-layer MoS<sub>2</sub> phototransistors. *ACS Nano* **2012**, *6*, 74–80. [[CrossRef](#)] [[PubMed](#)]
32. Wu, C.-C.; Jariwala, D.; Sangwan, V.K.; Marks, T.J.; Hersam, M.C.; Lauhon, L.J. Elucidating the photoresponse of ultrathin MoS<sub>2</sub> field-effect transistors by scanning photocurrent microscopy. *J. Phys. Chem. Lett.* **2013**, *4*, 2508–2513. [[CrossRef](#)]
33. Buscema, M.; Barkelid, M.; Zwiller, V.; van der Zant, H.S.J.; Steele, G.A.; Castellanos-Gomez, A. Large and tunable photothermoelectric effect in single-layer MoS<sub>2</sub>. *Nano Lett.* **2013**, *13*, 358–363. [[CrossRef](#)] [[PubMed](#)]
34. Pospischil, A.; Furchi, M.M.; Mueller, T. Solar-energy conversion and light emission in an atomic monolayer p-n diode. *Nat. Nanotechnol.* **2014**, *9*, 257–261. [[CrossRef](#)] [[PubMed](#)]
35. Baugher, B.W.H.; Churchill, H.O.H.; Yang, Y.; Jariwala, P. Optoelectronic devices based on electrically tunable p-n diodes in a monolayer dichalcogenide. *Nat. Nanotechnol.* **2014**, *9*, 262–267. [[CrossRef](#)] [[PubMed](#)]
36. Furchi, M.M.; Pospischil, A.; Libisch, F.; Burgdörfer, J.; Mueller, T. Photovoltaic effect in an electrically tunable van der Waals heterojunction. *Nano Lett.* **2014**, *14*, 4785–4791. [[CrossRef](#)] [[PubMed](#)]
37. Lee, C.-H.; Lee, G.-H.; van der Zande, A.M.; Chen, W.; Li, Y.; Han, M.; Cui, X.; Arefe, G.; Nuckolls, C.; Heinz, T.F.; *et al.* Atomically thin p-n junctions with van der Waals heterointerfaces. *Nat. Nanotechnol.* **2014**, *9*, 676–681. [[CrossRef](#)] [[PubMed](#)]
38. Fontana, M.; Deppe, T.; Boyd, A.K.; Rinzan, M.; Liu, A.Y.; Paranjape, M.; Barbara, P. Electron-hole transport and photovoltaic effect in gated MoS<sub>2</sub> Schottky junctions. *Sci. Rep.* **2013**, *3*. [[CrossRef](#)] [[PubMed](#)]
39. Dobusch, L.; Furchi, M.M.; Pospischil, A.; Mueller, T.; Bertagnolli, E.; Lugstein, A. Electric field modulation of thermovoltage in single-layer MoS<sub>2</sub>. *Appl. Phys. Lett.* **2014**, *105*. [[CrossRef](#)]
40. Lopez-Sanchez, O.; Lembke, D.; Kayci, M.; Radenovic, A.; Kis, A. Ultrasensitive photodetectors based on monolayer MoS<sub>2</sub>. *Nat. Nanotechnol.* **2013**, *8*, 497–501. [[CrossRef](#)] [[PubMed](#)]
41. Furchi, M.M.; Polyushkin, D.K.; Pospischil, A.; Mueller, T. Mechanisms of photoconductivity in atomically thin MoS<sub>2</sub>. *Nano Lett.* **2014**, *14*, 6165–6170. [[CrossRef](#)] [[PubMed](#)]
42. Zhang, W.; Huang, J.-K.; Chen, C.-H.; Chang, Y.-H.; Cheng, Y.-J.; Li, L.-J. High-gain phototransistors based on a CVD MoS<sub>2</sub> monolayer. *Adv. Mater.* **2013**, *25*, 3456–3461. [[CrossRef](#)] [[PubMed](#)]
43. Lee, H.S.; Min, S.-W.; Chang, Y.-G.; Park, M.K.; Nam, T.; Kim, H.; Kim, J.H.; Ryu, S.; Im, S. MoS<sub>2</sub> nanosheet phototransistors with thickness-modulated optical energy gap. *Nano Lett.* **2012**, *12*, 3695–3700. [[CrossRef](#)] [[PubMed](#)]
44. Choi, W.; Cho, M.Y.; Konar, A.; Lee, J.H.; Cha, G.-B.; Hong, S.C.; Kim, S.; Kim, J.; Jena, D.; Joo, J.; *et al.* High-detectivity multilayer MoS<sub>2</sub> phototransistors with spectral response from ultraviolet to infrared. *Adv. Mater.* **2012**, *24*, 5832–5836. [[CrossRef](#)] [[PubMed](#)]
45. Tsai, D.S.; Liu, K.K.; Lien, D.-H.; Tsai, M.L.; Kang, C.-F.; Lin, C.-A.; Li, L.-J.; He, J.-H. Few-layer MoS<sub>2</sub> with high broadband photogain and fast optical switching for use in harsh environments. *ACS Nano* **2013**, *7*, 3905–3911. [[CrossRef](#)] [[PubMed](#)]
46. Perea-López, N.; Perea-López, N.; Elías, A.N.; Berkdemir, A.; Castro-Beltran, A.; Gutiérrez, H.R.; Feng, S.; Lv, R.; Hayashi, T.; López-Urías, F.; *et al.* Photosensor device based on few-layered WS<sub>2</sub> films. *Adv. Funct. Mater.* **2013**, *23*, 5511–5517. [[CrossRef](#)]
47. Buscema, M.; Groenendijk, D.J.; Blanter, S.I.; Steele, G.A.; van der Zant, H.S.J.; Castellanos-Gomez, A. Fast and broadband photoresponse of few-layer black phosphorus field-effect transistors. *Nano Lett.* **2014**, *14*, 3347–3352. [[CrossRef](#)] [[PubMed](#)]
48. Liu, F.; Shimotani, H.; Shang, H.; Kanagasekaran, T.; Zólyomi, V.; Drummond, N.; Falko, V.I.; Tanigaki, K. High-sensitivity photodetectors based on multilayer GaTe flakes. *ACS Nano* **2014**, *8*, 752–760. [[CrossRef](#)] [[PubMed](#)]
49. Hu, P.; Wen, Z.; Wang, L.; Tan, P.; Xiao, K. Synthesis of few-layer GaSe nanosheets for high performance photodetectors. *ACS Nano* **2012**, *6*, 5988–5994. [[CrossRef](#)] [[PubMed](#)]
50. Hu, P.; Wang, L.; Yoon, M.; Zhang, J.; Feng, W.; Wang, X.; Wen, Z.; Idrobo, J.C.; Miyamoto, Y.; Geohagan, D.B.; *et al.* Highly responsive ultrathin GaS nanosheet photodetectors on rigid and flexible substrates. *Nano Lett.* **2013**, *13*, 1649–1654. [[CrossRef](#)] [[PubMed](#)]

51. Jacobs-Gedrim, R.B.; Shanmugam, M.; Jain, N.; Durcan, C.A.; Murphy, M.T.; Murray, T.M.; Matyi, R.J.; Moorell, R.J.; Yu, B. Extraordinary photoresponse in two-dimensional  $\text{In}_2\text{Se}_3$  nanosheets. *ACS Nano* **2014**, *8*, 514–521. [[CrossRef](#)] [[PubMed](#)]
52. Abderrahmane, A.; Ko, P.J.; Thu, T.V.; Ishizawa, S.; Takamura, T.; Sandhu, A. High photosensitivity few-layered  $\text{MoSe}_2$  back-gated field-effect phototransistors. *Nanotechnol.* **2014**, *25*. [[CrossRef](#)] [[PubMed](#)]
53. Kang, H.-S.; Choi, C.-S.; Choi, W.-Y.; Kim, D.-H.; Seo, K.-S. Characterization of phototransistor internal gain in metamorphic high-electron-mobility transistors. *Appl. Phys. Lett.* **2004**, *84*. [[CrossRef](#)]
54. Kufer, D.; Konstantatos, G. Highly sensitive, encapsulated  $\text{MoS}_2$  Photodetector with gate controllable gain and speed. *Nano Lett.* **2015**, *15*, 7307–7313.
55. Konstantatos, G.; Badioli, M.; Gaudreau, L.; Osmond, J.; Bernechea, M.; de Arquer, F.P.G.; Gatti, F.; Koppens, F.H.L. Hybrid graphene-quantum dot phototransistors with ultrahigh gain. *Nat. Nanotechnol.* **2012**, *7*, 363–368. [[CrossRef](#)] [[PubMed](#)]
56. Roy, K.; Padmanabhan, M.; Goswami, S.; Sai, T.P.; Ramalingam, G.; Raghavan, S.; Ghosh, A. Graphene- $\text{MoS}_2$  hybrid structures for multifunctional photoresponsive memory devices. *Nat. Nanotechnol.* **2013**, *8*, 826–830. [[CrossRef](#)] [[PubMed](#)]
57. Kufer, D.; Nikitskiy, I.; Lasanta, T.; Navickaite, G.; Koppens, F.H.L.; Konstantatos, G. Hybrid 2D–0D  $\text{MoS}_2$ -PbS quantum dot photodetectors. *Adv. Mater.* **2015**, *27*, 176–180. [[CrossRef](#)] [[PubMed](#)]
58. Geim, A.K.; Grigorieva, I.V. Van der Waals heterostructures. *Nature* **2013**, *499*, 419–425. [[CrossRef](#)] [[PubMed](#)]
59. Yu, W.J.; Liu, Y.; Zhou, H.; Yin, A.; Li, Z.; Huang, Y.; Duan, X. Highly efficient gate-tunable photocurrent generation in vertical heterostructures of layered materials. *Nat. Nanotechnol.* **2013**, *8*, 952–958. [[CrossRef](#)] [[PubMed](#)]
60. Britnell, L.; Ribeiro, R.M.; Eckmann, A.; Jalil, R.; Belle, B.D.; Mishchenko, A.; Kim, Y.-J.; Gorbachev, R.V.; Georgiou, T.; Morozov, S.V.; *et al.* Strong light-matter interactions in heterostructures of atomically thin films. *Science* **2013**, *340*, 1311–1314. [[CrossRef](#)] [[PubMed](#)]
61. Yang, W.; Yang, H.; Qin, G.; Ma, Z.; Berggren, J.; Hammar, M.; Soref, R.; Zhou, W. Large-area InP-based crystalline nanomembrane flexible photodetectors. *Appl. Phys. Lett.* **2010**, *96*. [[CrossRef](#)]
62. Kautek, W. Electronic mobility anisotropy of layered semiconductors: Transversal photoconductivity measurements at n- $\text{MoSe}_2$ . *J. Phys. C Solid State Phys.* **1982**, *15*. [[CrossRef](#)]
63. Massicotte, M.; Schmidt, P.; Violla, F.; Schädler, K.G.; Reserbat-Plantey, A.; Watanabe, K.; Taniguchi, T.; Tielrooij, K.J.; Koppens, F.H.L. Picosecond photoresponse in van der Waals heterostructures. *Nat. Nanotechnol.* **2016**, *11*, 42–46. [[CrossRef](#)] [[PubMed](#)]
64. Li, D.; Cheng, R.; Zhou, H.; Wang, C.; Yin, A.; Chen, Y.; Weiss, N.O.; Huang, Y.; Duan, X. Electric-field-induced strong enhancement of electroluminescence in multilayer molybdenum disulfide. *Nat. Commun.* **2015**, *6*. [[CrossRef](#)] [[PubMed](#)]
65. Zhang, Y.J.; Oka, T.; Suzuki, R.; Ye, J.T.; Iwasa, Y. Electrically switchable chiral light-emitting transistor. *Science* **2014**, *344*, 725–728. [[CrossRef](#)] [[PubMed](#)]
66. Li, Z.; Ezhilarasu, G.; Chatzakis, I.; Dhall, R.; Chen, C.-C.; Cronin, S.B. Indirect band gap emission by hot electron injection in metal/ $\text{MoS}_2$  and metal/ $\text{WSe}_2$  heterojunctions. *Nano Lett.* **2015**, *15*, 3977–3982. [[CrossRef](#)] [[PubMed](#)]
67. Sundaram, R.S.; Engel, M.; Lombardo, A.; Krupke, R.; Ferrari, A.C.; Avouris, P.; Steiner, M. Electroluminescence in single layer  $\text{MoS}_2$ . *Nano Lett.* **2013**, *13*, 1416–1421. [[CrossRef](#)] [[PubMed](#)]
68. Chen, J.; Perebeinos, V.; Freitag, M.; Tsang, J.; Fu, Q.; Liu, J.; Avouris, P. Bright infrared emission from electrically induced excitons in carbon nanotubes. *Science* **2005**, *310*, 1171–1174. [[CrossRef](#)] [[PubMed](#)]
69. Doh, Y.-J.; Maher, K.N.; Ouyang, L.; Yu, C.L.; Park, H.; Park, J. Electrically driven light emission from individual CdSe nanowires. *Nano Lett.* **2008**, *8*, 4552–4556. [[CrossRef](#)] [[PubMed](#)]
70. Ponomarev, E.; Gutierrez-Lezama, I.; Ubrig, N.; Morpurgo, A.F. Ambipolar light-emitting transistors on chemical vapor deposited monolayer  $\text{MoS}_2$ . *Nano Lett.* **2015**, *15*, 8289–8294. [[CrossRef](#)] [[PubMed](#)]
71. Choi, M.S.; Qu, D.; Lee, D.; Liu, X.; Watanabe, K.; Taniguchi, T.; Yoo, W.J. Lateral  $\text{MoS}_2$  p-n junction formed by chemical doping for use in high-performance optoelectronics. *ACS Nano* **2014**, *8*, 9332–9340. [[CrossRef](#)] [[PubMed](#)]
72. Ross, J.S.; Klement, P.; Jones, A.M.; Ghimire, N.J.; Yan, J.; Mandrus, D.G.; Taniguchi, T.; Watanabe, K.; Kitamura, K.; Yao, W.; *et al.* Electrically tunable excitonic light-emitting diodes based on monolayer  $\text{WSe}_2$  p-n junctions. *Nat. Nanotechnol.* **2014**, *9*, 268–272. [[CrossRef](#)] [[PubMed](#)]

73. Jo, S.; Ubrig, N.; Berger, H.; Kuzmenko, A.B.; Morpurgo, A.F. Mono- and bilayer WS<sub>2</sub> light-emitting transistors. *Nano Lett.* **2014**, *14*, 2019–2025. [[CrossRef](#)] [[PubMed](#)]
74. Lopez-Sanchez, O.; Llado, E.A.; Koman, V.; Fontcuberta i Morral, A.; Radenovic, A.; Kis, A. Light generation and harvesting in a van der Waals heterostructure. *ACS Nano* **2014**, *8*, 3042–3048. [[CrossRef](#)] [[PubMed](#)]
75. Withers, F.; del Pozo-Zamudio, O.; Mishchenko, A.; Rooney, A.P.; Gholinia, A.; Watanabe, K.; Taniguchi, T.; Haigh, S.J.; Geim, A.K.; Tartakovskii, A.I.; *et al.* Light-emitting diodes by band-structure engineering in van der Waals heterostructures. *Nat. Mater.* **2015**, *14*, 301–306. [[CrossRef](#)] [[PubMed](#)]
76. Ye, Y.; Ye, Z.; Gharghi, M.; Zhu, H.; Zhao, M.; Yin, X.; Zhang, X. Exciton-related electroluminescence from monolayer MoS<sub>2</sub>. *Appl. Phys. Lett.* **2014**, *104*. [[CrossRef](#)]
77. Withers, F.; del Pozo-Zamudio, O.; Schwarz, S.; Dufferwiel, S.; Walker, P.M.; Godde, T.; Rooney, A.P.; Gholinia, A.; Woods, C.R.; Blake, P.; *et al.* WSe<sub>2</sub> light-emitting tunneling transistors with enhanced brightness at room temperature. *Nano Lett.* **2015**, *15*, 8223–8228. [[CrossRef](#)] [[PubMed](#)]
78. Schwarz, S.; Dufferwiel, S.; Walker, P.M.; Withers, F.; Trichet, A.A.P.; Sich, M.; Li, F.; Chekhovich, E.A.; Borisenko, D.N.; Kolesnikov, N.N.; *et al.* Two-dimensional metal-chalcogenide films in tunable optical microcavities. *Nano Lett.* **2014**, *14*, 7003–7008. [[CrossRef](#)] [[PubMed](#)]
79. Wu, S.; Buckley, S.; Jones, A.M.; Ross, J.S.; Ghimire, N.J.; Yan, J.; Mandrus, D.G.; Yao, W.; Hatami, F.; Vučković, J.; *et al.* Control of two-dimensional excitonic light emission via photonic crystal. *2D Mater.* **2014**, *1*. [[CrossRef](#)]
80. Reed, J.C.; Zhu, A.Y.; Zhu, H.; Yi, F.; Cubukcu, E. Wavelength tunable microdisk cavity light source with a chemically enhanced MoS<sub>2</sub> emitter. *Nano Lett.* **2015**, *15*, 1967–1971. [[CrossRef](#)] [[PubMed](#)]
81. Wu, S.; Buckley, S.; Schaibley, J.R.; Feng, L.; Yan, J.; Mandrus, D.G.; Hatami, F.; Yao, W.; Vučković, J.; Majumdar, A.; *et al.* Monolayer semiconductor nanocavity lasers with ultralow thresholds. *Nature* **2015**, *520*, 69–72. [[CrossRef](#)] [[PubMed](#)]
82. Salehzadeh, O.; Djavid, M.; Tran, N.H.; Shih, I.; Mi, Z. Optically pumped two-dimensional MoS<sub>2</sub> lasers operating at room-temperature. *Nano Lett.* **2015**, *15*, 5302–5306. [[CrossRef](#)] [[PubMed](#)]
83. Ye, Y.; Wong, Z.J.; Lu, X.; Ni, X.; Zhu, H.; Chen, X.; Wang, Y.; Zhang, X. Monolayer excitonic laser. *Nat. Photonics* **2015**, *9*, 733–737. [[CrossRef](#)]
84. Tonndorf, P.; Schmidt, R.; Schneider, R.; Kern, J.; Buscema, M.; Steele, G.A.; Castellanos-Gomez, A.; van der Zant, H.S.J.; de Vasconcellos, S.M.; Bratschkitsch, R. Single-photon emission from localized excitons in an atomically thin semiconductor. *Optica* **2015**, *2*, 347–352. [[CrossRef](#)]
85. Srivastava, A.; Sidler, M.; Allain, A.V.; Lembke, D.S.; Kis, A.; Imamoglu, A. Optically active quantum dots in monolayer WSe<sub>2</sub>. *Nat. Nanotechnol.* **2015**, *10*, 491–496. [[CrossRef](#)] [[PubMed](#)]
86. He, Y.-M.; Clark, G.; Schaibley, J.R.; He, Y.; Chen, M.-C.; Wei, Y.-J.; Ding, X.; Zhang, Q.; Yao, W.; Xu, X.; *et al.* Single quantum emitters in monolayer semiconductors. *Nat. Nanotechnol.* **2015**, *10*, 497–502. [[CrossRef](#)] [[PubMed](#)]
87. Koperski, M.; Nogajewski, K.; Arora, A.; Cherkez, V.; Mallet, P.; Veuillen, J.Y.; Marcus, J.; Kossacki, P.; Potemski, M. Single photon emitters in exfoliated WSe<sub>2</sub> structures. *Nat. Nanotechnol.* **2015**, *10*, 503–506. [[CrossRef](#)] [[PubMed](#)]
88. Chakraborty, C.; Kinnischtzke, L.; Goodfellow, K.M.; Beams, R.; Vamivakas, A.N. Voltage-controlled quantum light from an atomically thin semiconductor. *Nat. Nanotechnol.* **2015**, *10*, 507–511. [[CrossRef](#)] [[PubMed](#)]
89. Palummo, M.; Bernardi, M.; Grossman, J.C. Exciton radiative lifetimes in two-dimensional transition metal dichalcogenides. *Nano Lett.* **2015**, *15*, 2794–2800. [[CrossRef](#)] [[PubMed](#)]
90. Tran, T.T.; Bray, K.; Ford, M.J.; Toth, M.; Aharonovich, I. Quantum emission from hexagonal boron nitride monolayers. *Nat. Nanotechnol.* **2015**, *11*, 37–41. [[CrossRef](#)] [[PubMed](#)]
91. Li, Y.; Chernikov, A.; Zhang, X.; Rigosi, A.; Hill, H.M.; van der Zande, A.M.; Chenet, D.A.; Shih, E.-M.; Hone, J.; Heinz, T.F. Measurement of the optical dielectric function of monolayer transition-metal dichalcogenides: MoS<sub>2</sub>, MoSe<sub>2</sub>, WS<sub>2</sub> and WSe<sub>2</sub>. *Phys. Rev. B* **2014**, *90*. [[CrossRef](#)]
92. Bernardi, M.; Palummo, M.; Grossman, J.C. Extraordinary sunlight absorption and one nanometer thick photovoltaics using two-dimensional monolayer materials. *Nano Lett.* **2013**, *13*, 3664–3670. [[CrossRef](#)] [[PubMed](#)]
93. Gan, L.-Y.; Zhang, Q.; Cheng, Y.; Schwingenschlöggl, U. Photovoltaic heterojunctions of fullerenes with MoS<sub>2</sub> and WS<sub>2</sub> monolayers. *J. Phys. Chem. Lett.* **2014**, *5*, 1445–1449. [[CrossRef](#)] [[PubMed](#)]

94. Echtermeyer, T.J.; Britnell, L.; Jasnós, P.K.; Lombardo, A.; Gorbachev, R.V.; Grigorenko, A.N.; Geim, A.K.; Ferrari, A.C.; Novoselov, K.S. Strong plasmonic enhancement of photovoltage in graphene. *Nat. Commun.* **2011**, *2*. [[CrossRef](#)] [[PubMed](#)]
95. Clemen, C.; Saldana, X.I.; Munz, P.; Bucher, E. Photovoltaic properties of some semiconducting layer structures. *Phys. Status Solidi A* **1978**, *49*, 437–443. [[CrossRef](#)]
96. Memaran, S.; Pradhan, N.R.; Lu, Z.; Rhodes, D.; Ludwig, J.; Zhou, Q.; Ogunolu, O.; Ajayan, P.M.; Smirnov, D.; Fernandez-Dominguez, A.I.; *et al.* Pronounced photovoltaic response from multilayered transition-metal Dichalcogenides PN-Junctions. *Nano Lett.* **2015**, *15*, 7532–7538. [[CrossRef](#)] [[PubMed](#)]
97. Groenendijk, D.J.; Buscema, M.; Steele, G.A.; de Vasconcellos, S.M.; Bratschitsch, R.; van der Zant, H.S.J.; Castellanos-Gomez, A. Photovoltaic and photothermoelectric effect in a double-gated WSe<sub>2</sub> device. *Nano Lett.* **2014**, *14*, 5846–5852. [[CrossRef](#)] [[PubMed](#)]
98. Buscema, M.; Groenendijk, D.J.; Steele, G.A.; van der Zant, H.S.J.; Castellanos-Gomez, A. Photovoltaic effect in few-layer black phosphorus PN junctions defined by local electrostatic gating. *Nat. Commun.* **2014**, *5*. [[CrossRef](#)] [[PubMed](#)]
99. Flöry, N.; Jain, A.; Bharadwaj, P.; Parzefall, M.; Taniguchi, T.; Watanabe, K.; Novotny, L. A WSe<sub>2</sub>/MoSe<sub>2</sub> heterostructure photovoltaic device. *Appl. Phys. Lett.* **2015**, *107*. [[CrossRef](#)]
100. Cheng, R.; Li, D.; Zhou, H.; Wang, C.; Yin, A.; Jiang, S.; Liu, Y.; Chen, Y.; Huang, Y.; Duan, X. Electroluminescence and photocurrent generation from atomically sharp WSe<sub>2</sub>/MoS<sub>2</sub> heterojunction p-n Diodes. *Nano Lett.* **2014**, *14*, 5590–5597. [[CrossRef](#)] [[PubMed](#)]
101. Hong, X.; Kim, J.; Shi, S.F.; Zhang, Y.; Jin, C.; Sun, Y.; Tongay, S.; Wu, J.; Zhang, Y.; Wang, F. Ultrafast charge transfer in atomically thin MoS<sub>2</sub>/WS<sub>2</sub> heterostructures. *Nat. Nanotechnol.* **2014**, *9*, 682–686. [[CrossRef](#)] [[PubMed](#)]
102. Rivera, P.; Schaibley, J.R.; Jones, A.M.; Ross, J.S.; Wu, S.; Aivazian, G.; Klement, P.; Seyler, K.L.; Clark, G.; Ghimire, N.J.; *et al.* Observation of long-lived interlayer excitons in monolayer MoSe<sub>2</sub>–WSe<sub>2</sub> heterostructures. *Nat. Commun.* **2015**, *6*. [[CrossRef](#)] [[PubMed](#)]
103. Yu, Y.; Hu, S.; Su, L.; Huang, L.; Liu, Y.; Jin, Z.; Purezky, A.A.; Geohegan, D.B.; Kim, K.W.; Zhang, Y.; *et al.* Equally efficient interlayer exciton relaxation and improved absorption in epitaxial and nonepitaxial MoS<sub>2</sub>/WS<sub>2</sub> heterostructures. *Nano Lett.* **2015**, *15*, 486–491. [[CrossRef](#)] [[PubMed](#)]
104. Wang, F.; Wang, Z.; Xu, K.; Wang, F.; Wang, Q.; Huang, Y.; Yin, L.; He, J. Tunable GaTe–MoS<sub>2</sub> van der Waals p-n Junctions with novel optoelectronic performance. *Nano Lett.* **2015**, *15*, 7558–7566. [[CrossRef](#)] [[PubMed](#)]
105. Cheng, H.-C.; Wang, G.; Li, D.; He, Q.; Yin, A.; Liu, Y.; Wu, H.; Ding, M.; Huang, Y.; Duan, X. van der Waals heterojunction devices based on organohalide perovskites and two-dimensional materials. *Nano Lett.* **2016**, *16*, 367–373. [[CrossRef](#)] [[PubMed](#)]
106. Wi, S.; Chen, M.; Li, D.; Nam, H.; Meyhofer, E.; Liang, X. Photovoltaic response in pristine WSe<sub>2</sub> layers modulated by metal-induced surface-charge-transfer doping. *Appl. Phys. Lett.* **2015**, *107*. [[CrossRef](#)]
107. Velez, S.; Ciudad, D.; Island, J.; Buscema, M.; Txoperena, O.; Parui, S.; Steele, G.A.; Casanova, F.; van der Zant, H.S.J.; Castellanos-Gomez, A.; *et al.* Gate-tunable diode and photovoltaic effect in an organic-2D layered material p-n junction. *Nanoscale* **2015**, *7*, 15442–15449. [[CrossRef](#)] [[PubMed](#)]
108. He, D.; Pan, Y.; Nan, H.; Gu, S.; Yang, Z.; Wu, B.; Luo, X.; Xu, B.; Zhang, Y.; Li, Y.; *et al.* A van der Waals p-n heterojunction with organic/inorganic semiconductors. *Appl. Phys. Lett.* **2015**, *107*. [[CrossRef](#)]
109. Jariwala, D.; Howell, S.L.; Chen, K.-S.; Kang, J.; Sangwan, V.K.; Filippone, S.A.; Turrissi, R.; Marks, T.J.; Lauhon, L.J.; Hersam, M.C. Hybrid, gate-tunable, van der Waals p-n heterojunctions from pentacene and MoS<sub>2</sub>. *Nano Lett.* **2015**, *16*, 497–503. [[CrossRef](#)] [[PubMed](#)]
110. Xu, X.; Yao, W.; Xiao, D.; Heinz, T.F. Spin and pseudospins in layered transition metal dichalcogenides. *Nat. Phys.* **2014**, *10*, 343–350. [[CrossRef](#)]
111. Zeng, H.; Dai, J.; Yao, W.; Xiao, D.; Cui, X. Valley polarization in MoS<sub>2</sub> monolayers by optical pumping. *Nat. Nanotechnol.* **2012**, *7*, 490–493. [[CrossRef](#)] [[PubMed](#)]
112. Cao, T.; Wang, G.; Han, W.; Ye, H.; Zhu, C.; Shi, J.; Niu, Q.; Tan, P.; Wang, E.; Liu, B.; *et al.* Valley-selective circular dichroism of monolayer molybdenum disulfide. *Nat. Commun.* **2012**, *3*. [[CrossRef](#)] [[PubMed](#)]
113. Srivastava, A.; Sidler, M.; Allain, A.V.; Lembke, D.S.; Kis, A.; Imamoglu, A. Valley Zeeman effect in elementary optical excitations of monolayer WSe<sub>2</sub>. *Nat. Phys.* **2015**, *11*, 141–147. [[CrossRef](#)]
114. Mak, K.F.; McGill, K.L.; Park, J.; McEuen, P.L. The valley Hall effect in MoS<sub>2</sub> transistors. *Science* **2014**, *344*, 1489–1492. [[CrossRef](#)] [[PubMed](#)]

115. Eginligil, M.; Cao, B.; Wang, Z.; Shen, X.; Cong, C.; Shang, J.; Soci, C.; Yu, T. Dichroic spin-valley photocurrent in monolayer molybdenum disulphide. *Nat. Commun.* **2015**, *6*. [[CrossRef](#)] [[PubMed](#)]
116. Yuan, H.; Wang, X.; Lian, B.; Zhang, H.; Fang, X.; Shen, B.; Xu, G.; Xu, Y.; Zhang, S.-C.; Hwang, H.Y.; *et al.* Generation and electric control of spin–valley-coupled circular photogalvanic current in WSe<sub>2</sub>. *Nat. Nanotechnol.* **2014**, *9*, 851–857. [[CrossRef](#)] [[PubMed](#)]
117. Zhan, Y.; Liu, Z.; Najmaei, S.; Ajayan, P.M.; Lou, J. Large-area vapor-phase growth and characterization of MoS<sub>2</sub> atomic layers on a SiO<sub>2</sub> substrate. *Small* **2012**, *8*, 966–971. [[CrossRef](#)] [[PubMed](#)]
118. Yu, Y.; Li, C.; Liu, Y.; Su, L.; Zhang, Y.; Cao, L. Controlled scalable synthesis of uniform, high-quality monolayer and few-layer MoS<sub>2</sub> films. *Sci. Rep.* **2013**, *3*. [[CrossRef](#)] [[PubMed](#)]
119. Dumcenco, D.; Ovchinnikov, D.; Marinov, K.; Lazić, P.; Gibertini, M.; Marzari, N.; Sanchez, O.L.; Kung, Y.-C.; Krasnozhan, D.; Chen, M.-W.; *et al.* Large-area epitaxial monolayer MoS<sub>2</sub>. *ACS Nano* **2015**, *9*, 4611–4620. [[CrossRef](#)] [[PubMed](#)]
120. Huang, J.-K.; Pu, J.; Hsu, C.-L.; Chiu, M.-H.; Juang, Z.-Y.; Chang, Y.-H.; Chang, W.-H.; Iwasa, Y.; Takenobu, T.; Li, L.-J. Large-area synthesis of highly crystalline WSe<sub>2</sub> monolayers and device applications. *ACS Nano* **2014**, *8*, 923–930. [[CrossRef](#)] [[PubMed](#)]
121. Wang, X.; Gong, Y.; Shi, G.; Chow, W.L.; Keyshar, K.; Ye, G.; Vajtai, R.; Lou, J.; Liu, Z.; Ringe, E.; *et al.* Chemical vapor deposition growth of crystalline monolayer MoSe<sub>2</sub>. *ACS Nano* **2014**, *8*, 5125–5131. [[CrossRef](#)] [[PubMed](#)]
122. Huang, C.; Wu, S.; Sanchez, A.M.; Peters, J.J.P.; Beanland, R.; Ross, J.S.; Rivera, P.; Yao, W.; Cobden, D.H.; Xu, X. Lateral heterojunctions within monolayer MoSe<sub>2</sub>–WSe<sub>2</sub> semiconductors. *Nat. Mater.* **2014**, *13*, 1096–1101. [[CrossRef](#)] [[PubMed](#)]
123. Li, J.; Östling, M. Scalable Fabrication of 2D Semiconducting crystals for future electronics. *Electronics* **2015**, *4*, 1033–1061. [[CrossRef](#)]
124. Kang, K.; Xie, S.; Huang, L.; Han, Y.; Huang, P.Y.; Mak, K.F.; Kim, C.-J.; Muller, D.; Park, J. High-mobility three-atom-thick semiconducting films with wafer-scale homogeneity. *Nature* **2015**, *520*, 656–660. [[CrossRef](#)] [[PubMed](#)]
125. Li, M.-Y.; Shi, Y.; Cheng, C.-C.; Lu, L.-S.; Lin, Y.-C.; Tang, H.-L.; Tsai, M.-L.; Chu, C.-W.; Wei, K.-H.; He, J.-H.; *et al.* Epitaxial growth of a monolayer WSe<sub>2</sub>–MoS<sub>2</sub> lateral p–n junction with an atomically sharp interface. *Science* **2015**, *349*, 524–528. [[CrossRef](#)] [[PubMed](#)]
126. Lin, Z.; Zhao, Y.; Zhou, C.; Zhong, R.; Wang, X.; Tsang, Y.H.; Chai, Y. Controllable growth of large-size crystalline MoS<sub>2</sub> and resist-free transfer assisted with a Cu thin film. *Sci. Rep.* **2015**, *5*. [[CrossRef](#)] [[PubMed](#)]
127. Gong, Y.; Lin, J.; Wang, X.; Shi, G.; Lei, S.; Lin, Z.; Zou, X.; Ye, G.; Vajtai, R.; Yakobson, B.I.; *et al.* Vertical and in-plane heterostructures from WS<sub>2</sub>/MoS<sub>2</sub> monolayers. *Nat. Mater.* **2014**, *13*, 1135–1142. [[CrossRef](#)] [[PubMed](#)]

